www.springer.com/41230
https://doi.org/10.1007/s41230-026-5185-3

Optimization of multi-process parameters in secondary cooling solidification process of S30432 continuous casting billet

Zhi-qiang Li[1, 2], Ying-xuan Shan[1, 6], Li Wu[1, 2], Hua Hou[1, 2, 5], and *Yu-hong Zhao[1, 2, 3, 4]

1. School of Materials Science and Engineering, Collaborative Innovation Center of Ministry of Education and Shanxi Province for High-performance Al/Mg Alloy Materials, North University of China, Taiyuan 030051, China

2. School of Materials Science and Engineering, Key Laboratory of Advanced Forming of New Materials Intelligent Casting, Shanxi Province, North University of China, Taiyuan 030051, China

3. Beijing Advanced Innovation Center for Materials Genome Engineering, University of Science and Technology Beijing, Beijing 100083, China

4. Institute of Materials Intelligent Technology, Liaoning Academy of Materials, Shenyang 110004, China

5. School of Materials Science and Engineering, Taiyuan University of Science and Technology, Taiyuan 030024, China

6. Inner Mongolia North Heavy Industries Group Co., Ltd., Baotou 014000, Inner Mongolia, China

Abstract: The synergistic mechanism of multiple process parameters on the solidification structure of niobium containing austenitic stainless steel during continuous casting is complex, which seriously affects the quality of continuous casting billets and seamless pipes. In order to optimize the quality of continuous casting billet, a finite element model of solidification and heat transfer in continuous casting process was established for the secondary cooling process of continuous casting billet. The control variable method was used to explore the influence of casting speed and superheat on the solidification process. At the same time, an orthogonal scheme was designed to study the coupling effect of multiple process parameters on the heat transfer and solidification state of continuous casting billets, and optimized process parameters were selected. The optimization results of process parameters were verified through production experiments, and it is found that the enrichment of coarse niobium compounds directly causes the initiation and propagation of inner wall cracks during the large deformation hot piercing of S30432 seamless tubes. Process parameter optimization, especially the synergistic effect of the decrease of superheat and increase of specific water flow promotes the grain refinement and expension of equiaxed crystal zone, thereby mitigating the segregation of Nb elements and improving the distribution of niobium compounds.

Keywords: continuous casting; solidification process; process parameter optimization; niobium compounds; crack

CLC numbers: TG142.71 **Document code:** A **Article ID:** 1672-6421(2026)03-407-14

1 Introduction

Austenitic heat-resistant stainless steel has become an important choice for seamless steel tubes of supercritical and ultra-supercritical power station boilers due to its excellent high temperature stability[1-3]. However, due to the solidification conditions of the continuous casting process and the low solute balance distribution coefficient of Nb element, serious grain boundary segregation occurs in the solidified structure of S30432 with a high Nb content, forming a large amount of unevenly distributed niobium compounds, which greatly reduces the quality and hot working performance of the billet, and leads to the formation of pores and initiation of cracks[4]. Moreover, the bulk NbC primary phase is difficult to be removed by subsequent heat treatment. Therefore, it is urgent to find a method to control the quality of continuous casting billets and seamless tubes.

***Yu-hong Zhao**

Ph. D. Supervisor. She mainly engages in the design of high-performance alloys and the development of equipment for liquid/semi-solid forming processes, as well as research on process software integration technology.

E-mail: zhaoyuhong@nuc.edu.cn

Received: 2025-08-06; Revised: 2025-12-03; Accepted: 2026-05-12

The current research has gradually realized the regulation of solute element distribution in the solidification process of continuous casting through thermodynamic design, refinement of process parameters, and auxiliary technological innovation[5-9]. Researchers often improve billet quality by optimizing the relevant modules of the continuous casting process, such as immersion nozzle structure and immersion depth[10-12], distribution of mould fluxes[13, 14], mold structure and vibration frequency[15], electromagnetic stirring parameters[16-23], secondary cooling water[24-29], casting speed[30-32], superheat[33, 34] and continuous casting supporting equipment[35]. In addition, the optimization of alloy composition design combined with thermodynamic calculation is also an important aspect[36-40]. For example, the precipitation kinetics of Nb(C, N) can be controlled by changing the content of C, N, and Nb elements, which can weaken the tendency of element segregation to a certain extent. However, the accuracy of alloy composition design optimization is attributed to the accuracy of the phase diagram calculation database and how to consider the interaction between a large number of alloy elements[41, 42]. In addition, it is also necessary to maintain the service performance and production cost of the alloy in its operating environment[43-45]. Therefore, in the actual production process, it is difficult to optimize the quality of the billet by directly changing the composition.

In the actual continuous casting production process, the molten steel needs to pass through the mold, the foot roller zone, the secondary cooling zone, and the air cooling zone. For a specific alloy type, its melting process, refining process, nozzle setting, mold and other related device settings are relatively certain, and the main parameters that have a greater impact on the actual billet microstructure are related to a series of solidification events such as the microstructure of the billet from nucleation to growth, and then to grain shape transformation[46]. Process parameters such as casting speed, superheat, secondary cooling water distribution, and their coupling effect, directly regulate the solidification kinetics of the billet. This is reflected in the nucleation and growth process, mainly in the nucleation undercooling, temperature gradient, cooling rate, and growth rate[47, 48]. The change of macro process parameters directly affects the change of nucleation and growth parameters of these structures, which leads to the formation of different fine grain zone, columnar crystal zone, equiaxed crystal zone, and element segregation. Therefore, the influence of the above key continuous casting parameters on the parameters related to the nucleation of the solidified structure should be considered, and the coupling effect between the process parameters should be related to the solidification state and microstructural distribution, so as to further clarify the synergistic mechanism among the multiple process parameters.

Therefore, in this study, the coupling optimization of multi-process parameters of continuous casting was carried out to address piercing cracks in S30432 billets and seamless tubes. The process parameters such as casting speed, superheat, and gradient design of secondary cooling zone were simulated and studied. The temperature field, solidification process, and microstructure evolution of continuous casting billets under the action of single and coupled process parameters were analyzed, and the causes and solutions of defects in billets and seamless tubes were revealed, which provide reference for the optimization of process parameters in actual production process.

2 Methods

2.1 Modeling

The mature finite element simulation software Ansys was used to simulate the solidification process of continuous casting. Based on the symmetry of heat transfer during the cooling process of continuous casting billet, a two-dimensional slice model representing the cross section of a quarter billet was established using the two-dimensional slice method. The schematic of the continuous casting process and the position of each cooling section are shown in Fig. 1.

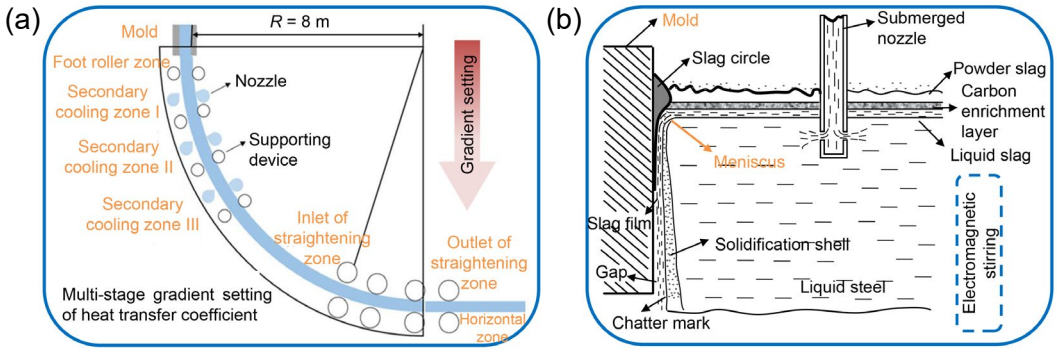

(c)

Cooling zone	Mold zone	Foot roller zone	Secondary cooling zone I	Secondary cooling zone II	Secondary cooling zone III
Zone length (m)	0.66	0.62	1.7	2	2.3

Cooling zone	Inlet of straightening zone	Outlet of straightening zone	End of horizontal zone
Distance to the meniscus (m)	8.48	13.64	17.69

Fig. 1: Continuous casting model diagram (a), structure diagram near the meniscus (b), and the length and position parameters of each zone of continuous casting model (c)

The cooling scheme of the secondary cooling zone was mainly carried out in a weak cooling mode. The heat transfer coefficient of the secondary cooling zone was used to reflect the water distribution during each stage of the secondary cooling, and the heat transfer coefficient was set in a multi-stage gradient. For the conversion of heat transfer coefficient and secondary cooling water quantity, firstly, the total water quantity of the secondary cooling zone was calculated by the preset specific water flow, and then the water quantity of each section was calculated according to the water distribution equation. Finally, the heat transfer coefficient of each secondary cooling zone was calculated by the heat transfer coefficient equation, so as to be applied to the subsequent calculation.

The total water quantity in the secondary cooling zone can be calculated according to the following equation[49]:

$$Q = a \cdot b \cdot \rho \cdot \vartheta \cdot f \tag{1}$$

where Q is the total water quantity in the secondary cooling zone, L·min^{-1}; $a \cdot b$ is the section size of the billet, m^2; f is specific water flow, L·kg^{-1}; ϑ is the casting speed, m·min^{-1}; and ρ is the billet density, kg·mm^{-3}.

The secondary cooling stage is divided into four sections, and the water distribution mode of each section is[49]:

$$Q_0 : Q_1 : Q_2 : Q_3 = \frac{1}{\sqrt{S_0}} : \frac{1}{\sqrt{S_1}} : \frac{1}{\sqrt{S_2}} : \frac{1}{\sqrt{S_3}} \tag{2}$$

The total water quantity is:

$$Q = Q_0 + Q_1 + Q_2 + Q_3 \tag{3}$$

Due to

$$\Sigma \frac{1}{\sqrt{S_i}} = \frac{1}{\sqrt{S_0}} + \frac{1}{\sqrt{S_1}} + \frac{1}{\sqrt{S_2}} + \frac{1}{\sqrt{S_3}} \tag{4}$$

Then

$$Q_0 = \frac{Q}{\sqrt{S_0} \times \Sigma \frac{1}{\sqrt{S_i}}},\ Q_1 = \frac{Q}{\sqrt{S_1} \times \Sigma \frac{1}{\sqrt{S_i}}}$$
$$Q_2 = \frac{Q}{\sqrt{S_2} \times \Sigma \frac{1}{\sqrt{S_i}}},\ Q_3 = \frac{Q}{\sqrt{S_3} \times \Sigma \frac{1}{\sqrt{S_i}}} \tag{5}$$

where S_i is the length from the liquid level of the mold to the cooling center point of each section.

During the simulation process, the heat transfer coefficient can be set according to an empirical equation suitable for austenitic stainless steel materials[49]:

$$h = 581 w^{0.451} (1 - 0.0075 T_w) \tag{6}$$

where T_w is the temperature of the cooling water, °C; w is the water flow density, L·(m^2·s)$^{-1}$; and h is the heat transfer coefficient, W·(m^2·°C)$^{-1}$.

The relationship between water flow density and water quantity can be calculated by the following equation:

$$w = DQ \tag{7}$$

where D is a coefficient related to the spray area of the casting billet. It can be calculated by combining Eq. (6) and Eq. (7).

$$w = 25.82 - 11.25 P^{-0.11} \tag{8}$$

where P is the water quantity sprayed onto the entire surface of the casting billet in the secondary cooling zone per unit time, L·(m^2·s)$^{-1}$.

The range of continuous casting process parameters selected in this study was as follows: the casting speed was 0.8–1.2 m·min^{-1}, the superheat was 10–50 °C, and the specific water flow was 0.1–0.5 L·kg^{-1}. The specific continuous casting secondary cooling process parameters and the corresponding heat transfer coefficient values are shown in Table 1.

2.2 Material parameters

The material used in the simulation was austenitic stainless steel S30432, and its chemical composition is shown in Table 2. The thermal physical parameters were calculated based on the Fe based database in Pandat software. The solidification process was calculated using the Scheil model, which is more closely related to the actual non-equilibrium solidification process in continuous casting[36]. The results are shown in Fig. 2.

2.3 Experiment and characterization

The vertical bending continuous casting machine was used to verify the production experiment. After melting and refining, S30432 alloy was injected into the tundish, and then the molten steel was distributed to three molds by the submerged nozzle. The surface layer of continuous casting billet solidified rapidly under the action of mold. Following the coordinated operation of the pulling straightening machine and the mold vibration device, the billet in the mold was pulled out. After secondary cooling and electromagnetic stirring, it was cut into a 2.5 m long square billet with a cross-sectional dimension of 220 mm×220 mm. During the secondary cooling stage, the gas-water atomization cooling with dynamic water distribution was used around the billet to achieve uniform cooling. Before hot rolling, the billet underwent surface treatment, and then heated to 1,200 °C within the furnace. After hot rolling and air cooling, the hot rolled round billet was reheated to 1,100 °C, and the seamless steel tube was obtained by piercing deformation process with two-roll cross piercing equipment. JSM-IT800 field emission scanning electron microscope was used to characterize the cross-section morphology and piercing structure of the billet before and after the optimization of continuous casting process parameters. EDS mapping was used to characterize the distribution of Nb element in the microstructure.

3 Results and discussion

3.1 Change of section temperature and shell thickness during solidification process of continuous casting billet

The solidification process of S30432 stainless steel billet was simulated under the conditions of casting speed of 0.9 m·min^{-1}, superheat of 20 °C, and specific water flow of 0.3 L·kg^{-1}. Figures 3(a)–(f) are the cloud diagram of the temperature field of the two-dimensional slice model of a quarter billet. It can be seen that the temperature in the core of the billet is the highest and that in the corner zone is the lowest. From the core of the billet to the corner, the temperature gradually decreases. The trend is due to the heat of the corner of the billet diverging in

Table 1: Continuous casting secondary cooling process parameters and the corresponding heat transfer coefficient values

Case	Casting speed ($m \cdot min^{-1}$)	Superheat (°C)	Specific water flow ($L \cdot kg^{-1}$)	Heat transfer coefficient [$W \cdot (m^2 \cdot °C)^{-1}$]			
				Foot roll zone	Secondary cooling zone I	Secondary cooling zone II	Secondary cooling zone III
Case 1	0.8	10	0.1	781.35	433.07	331.94	292.78
Case 2	0.8	20	0.2	924.77	512.33	392.58	346.85
Case 3	0.8	30	0.3	996.13	527.96	404.60	357.26
Case 4	0.8	40	0.4	1,042.42	581.26	445.46	393.24
Case 5	0.8	50	0.5	1,076.25	596.34	457.12	403.61
Case 6	0.9	10	0.1	808.05	447.54	343.37	303.12
Case 7	0.9	20	0.2	946.24	524.29	401.82	354.67
Case 8	0.9	30	0.3	1,015.47	562.72	431.31	380.72
Case 9	0.9	40	0.4	1,060.50	587.59	450.34	397.65
Case 10	0.9	50	0.5	1,093.44	605.89	464.39	410.04
Case 11	1.0	10	0.1	830.98	460.30	352.76	311.53
Case 12	1.0	20	0.2	964.99	534.66	409.84	361.73
Case 13	1.0	30	0.3	1,032.35	572.07	438.38	386.99
Case 14	1.0	40	0.4	1,076.25	596.34	457.12	403.61
Case 15	1.0	50	0.5	1,108.46	614.21	470.73	415.64
Case 16	1.1	10	0.1	851.05	471.47	361.37	319.33
Case 17	1.1	20	0.2	981.40	543.80	416.90	367.95
Case 18	1.1	30	0.3	1,047.25	580.20	444.77	392.71
Case 19	1.1	40	0.4	1,090.21	604.09	462.99	408.75
Case 20	1.1	50	0.5	1,121.71	621.57	476.34	420.60
Case 21	1.2	10	0.1	869.03	481.38	369.01	325.84
Case 22	1.2	20	0.2	996.13	551.94	422.98	373.49
Case 23	1.2	30	0.3	1,060.50	587.59	450.34	397.65
Case 24	1.2	40	0.4	1,102.67	611.01	468.24	413.46
Case 25	1.2	50	0.5	1,133.59	628.10	481.37	425.05

Table 2: Chemical composition of S30432 steel (wt.%)

Cr	Ni	Mn	Si	Nb	C	N	P	S	B	Cu	Fe
18.48	8.86	0.8	0.23	0.47	0.076	0.1	0.031	0.002	0.0034	2.8	Bal.

two directions and cooling faster. The temperature of the billet in the mold is instantaneously reduced by the quenching of the mold and the cooling water, forming an initial shell. As the continuous casting process continues, the billet solidifies from the corner and surface to the core until the temperature tends to be stable after complete solidification.

Figure 3(g) shows the temperature curves of the surface center and the core of the billet at the quarter section during the steady-state equilibrium of continuous casting. By monitoring and recording the temperature of the outlet characteristic points at each cooling stage of the billet surface of the three runners in actual production, it is found that the results are in good agreement with the simulation results, which verifies the accuracy of the proposed model and simulation method. It can be seen that the temperature of the two characteristic points in the surface center and corner of the billet shows a downward trend with the solidification process, and the temperature at the center of the billet decreases continuously. When the distance to

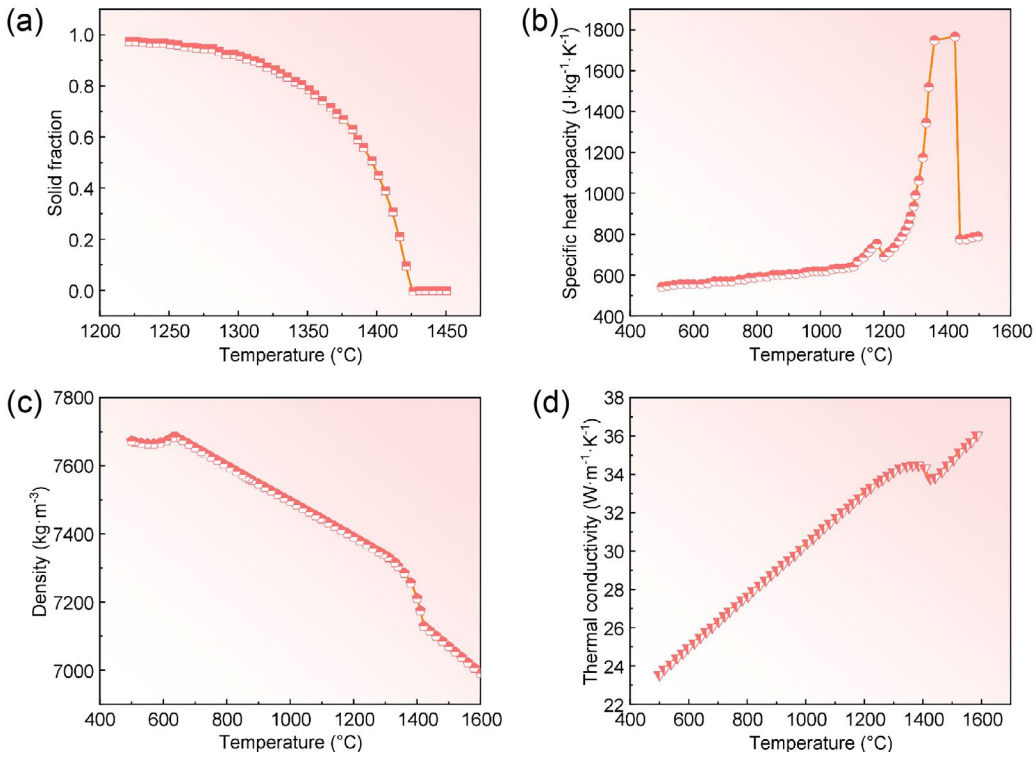

Fig. 2: Thermal physical parameters of S30432: (a) solid fraction; (b) specific heat capacity; (c) density; (d) thermal conductivity

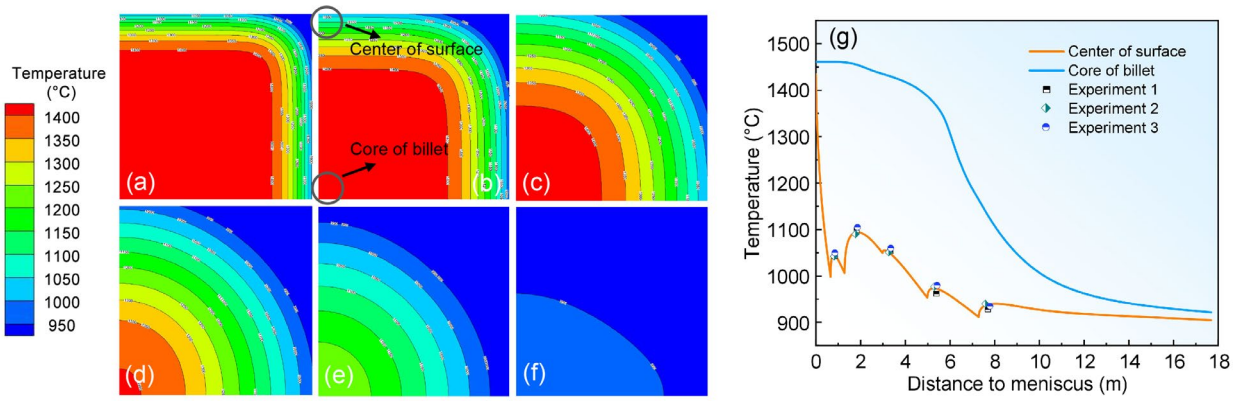

Fig. 3: Temperature change of quarter section in continuous casting process: (a) outlet of mold; (b) outlet of foot roller zone; (c) outlet of secondary cooling zone I; (d) outlet of secondary cooling zone II; (e) outlet of secondary cooling zone III; (f) outlet of straightening zone; (g) calculated temperature change curves of the center of billet surface and the core of billet and the experimental records

the menisus is 6.26 m, the temperature at the core of the billet decreases rapidly, mainly because the solidification latent heat of the molten steel inside the billet has been basically released, and the temperature at the core of the billet has dropped below the solidus temperature. The temperature at the center of the billet surface has different degrees of temperature recovery trend in special positions, which is mainly due to the change of heat transfer coefficient in each cooling stage of the billet. With the decrease of cooling intensity, the heat transferred to the surface of the billet in a short time is greater than the heat transferred from the surface to the outside, so that the surface temperature will increase in a short time, and then the temperature will continue to decrease under the cooling effect. When the rewarming amplitude is too large, the temperature is not uniform and cracks are easy to occur. Therefore, the design scheme should ensure that the recovery temperature is within a reasonable range as far as possible, and the value should be as small as possible.

Figure 4 indicates the shell thickness distribution of each stage of continuous casting under a casting speed of 0.9 $m \cdot min^{-1}$, a superheat of 20 °C, and a specific water flow of 0.3 $L \cdot kg^{-1}$. During the process of continuous casting, the molten steel undergoes chilling by the copper wall of the mold, and an initial solidified shell is quickly formed on the surface of the billet. Then, the high temperature liquid flows downward into the secondary cooling zone and the air cooling zone, and the billet begins to solidify from the surface of the billet to the core of the billet. At this time, the surface of the billet has solidified into a solid state, but the core is still a high temperature liquid, showing a 'V' shape of the molten steel,

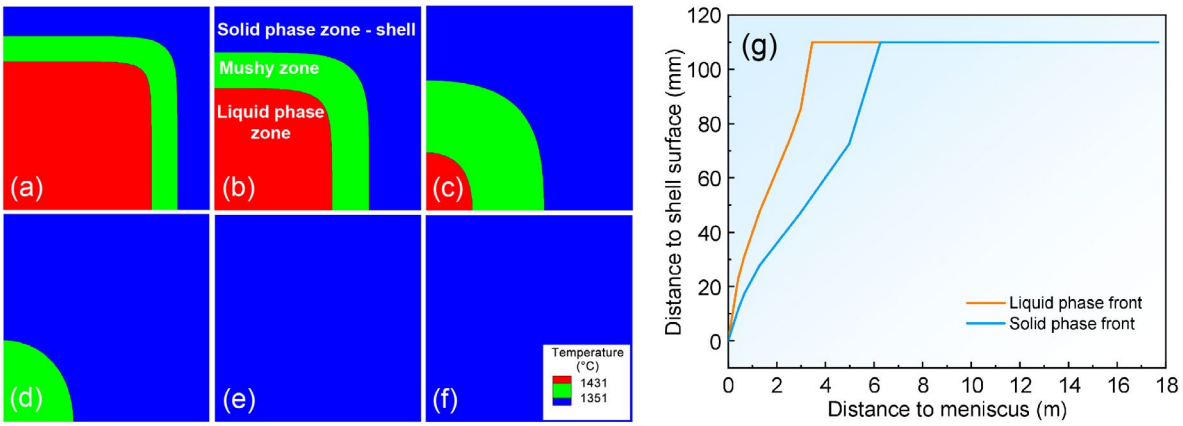

Fig. 4: Change of shell thickness in different stages of secondary cooling continuous casting process: (a) outlet of mold; (b) outlet of foot roller zone; (c) outlet of secondary cooling zone I; (d) outlet of secondary cooling zone II; (e) outlet of secondary cooling zone III; (f) outlet of straightening zone; (g) distance from the solid and liquid fronts to the surface of shell during solidification

that is, the liquid cavity. The blue, green, and red zones in Figs. 4(a)–(f) represent the solid shell, mushy zone, and liquid zone, respectively. In the actual solidification process of molten steel, the increase of mushy zone can easily lead to shrinkage porosity defects in the billet.

Figure 4(g) shows the distance change from the solid/liquid front to the surface of the shell during the solidification process. It can be seen from the curve that the growth of the solidified shell during the solidification process is mainly divided into three stages. Under the rapid cooling effect of mold and foot roll area at the initial stage of solidification, the surface of the billet rapidly solidifies into a shell, and the shell grows quickly. In the middle stage of solidification, the billet enters the first zone of secondary cooling, the second zone of secondary cooling and the third zone of secondary cooling successively. At this time, the cooling intensity is obviously weakened, the heat transfer coefficient is obviously reduced, and the growth of solidified shell gradually slows down. At the end of solidification, the latent heat of solidification gradually disappears, and the growth rate of the shell thickness of the billet is obviously accelerated at the end of solidification. From Fig. 4(g), it can be seen that the length of mushy zone is 2.45 m when the core temperature of the billet is lower than the liquidus temperature. In order to ensure the internal quality of continuous casting billet, the length of mushy zone should be as small as possible.

3.2 Effect of a single factor on solidification process of continuous casting billet

3.2.1 Casting speed

In order to explore the influence of casting speed on the solidification process of continuous casting, five groups of schemes were designed by the control variable method. The superheat was controlled to be 30 °C, and the casting speed was set to be 0.8 $m \cdot min^{-1}$, 0.9 $m \cdot min^{-1}$, 1.0 $m \cdot min^{-1}$, 1.1 $m \cdot min^{-1}$, and 1.2 $m \cdot min^{-1}$, respectively. The specific water flow was set to be 0.3 $L \cdot kg^{-1}$.

As shown in Fig. 5(a), when the two variables of specific water flow and superheat are the same, the overall change trend of the temperature at the center of the billet surface remains the same. However, at the same position from the meniscus of the mold, the temperature at surface center increases with the increase of the casting speed, and the outlet temperature of straightening zone are 914.03 °C, 975.56 °C, 1,027.6 °C, 1,072.3 °C, and 1,125.9 °C, respectively. That is, the larger the casting speed, the higher the surface temperature of the straightening zone. The overall trend in Fig. 5(b) indicates that the core temperature of the billet gradually decreases with the continuous casting process. When the billet reaches a steady state, at the same position from the meniscus of the mold, the core temperature at the same position increases with the increase of the casting speed.

The main reason for the above results is that although the specific water flow is the same, the heat transfer coefficient on the surface of the billet is different under different casting speeds. The data in Table 1 demonstrate the characteristics that the higher the casting speed, the higher the heat transfer coefficient, but the increase rate of casting speed is much higher than that of heat transfer coefficient. Therefore, the chilling effect caused by the increase of heat transfer coefficient may not be able to offset the slow cooling effect caused by the rapid increase of casting speed to a great extent. That is, the casting speed is too fast, but the corresponding heat transfer coefficient is not high enough, resulting in insufficient actual cooling intensity. This eventually leads to a delay in the solidification of molten steel under high casting speed conditions, resulting in a higher temperature in both the core and surface of the billet.

Figure 5(c) shows the change curves of solid/liquid front position during continuous casting at different casting speeds. As the casting speed increases from 0.8 $m \cdot min^{-1}$ to 1.2 $m \cdot min^{-1}$, the length of the mushy zone increases from 2.36 m to 4.37 m. When the casting speed increases by 0.1 $m \cdot min^{-1}$, the length difference of mushy zone also increases gradually, which is 0.42 m, 0.44 m, 0.48 m, and 0.67 m, respectively. With the increase of the casting speed, the length of the mushy zone increases. This is because as the casting speed increases, the time of the billet staying in each cooling zone becomes shorter.

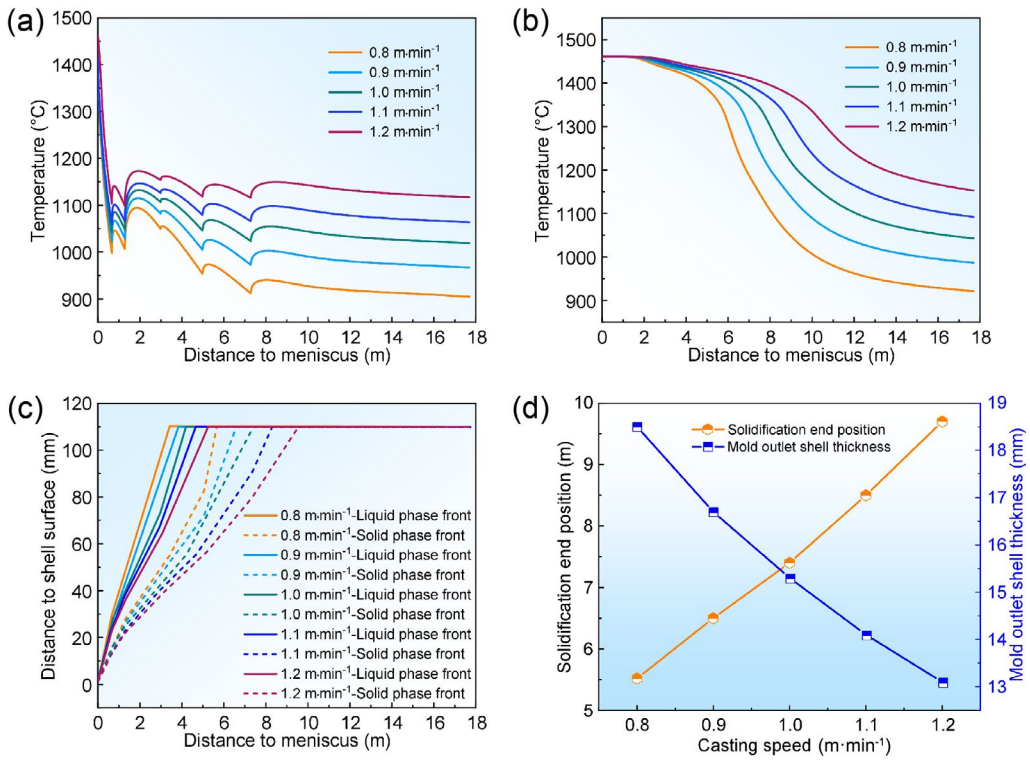

Fig. 5: Effect of casting speed on solidification process of continuous casting billet: (a) temperature change of surface center; (b) temperature change of billet core; (c) change of solid phase and liquid phase front position; (d) solidification end position and mold outlet shell thickness at different casting speeds

Even if the heat transfer coefficient increases, the actual increase is small, resulting in the actual cooling effect can not make up for the solidification delay caused by the increase of the casting speed. Figure 5(d) shows the changes of the solidification end position and the thickness of the solidified shell in the mold during the continuous casting process at different casting speeds. With the increase of casting speed, the residence time of the billet in the secondary cooling zone is shortened, and the billet can not be fully cooled, resulting in the position of the solidification end moving backward. The shell thickness at the mold outlet is mainly related to the casting speed and superheat. When the superheat is stable, the increase of casting speed reduces the residence time of molten steel in the mold, thereby the cooling effect is poor, which makes the shell thickness at the mold outlet decrease continuously.

In summary, when other conditions remain unchanged, the slower the casting speed, the better the cooling effect, the lower the temperature in the billet core and surface center. This leads to a shorter liquid cavity and mushy zone, a thicker solidified shell at the mold outlet, and ultimately improved billet quality. In the actual production process, the casting speed should be moderate. If the casting speed is too slow, the production efficiency will be too low. If the casting speed is too fast, it will easily lead to incomplete cooling of the billet and cause steel leakage.

3.2.2 Superheat

In order to explore the influence of superheat on the solidification process of continuous casting, five groups of schemes were designed by the control variable method. The casting speed was controlled to be 0.9 $m \cdot min^{-1}$, and the superheat was set to 10 °C, 20 °C, 30 °C, 40 °C, and 50 °C, respectively, and the specific water flow was 0.3 $L \cdot kg^{-1}$. As shown in Fig. 6(a), the overall trend of the temperature at the center of the billet surface remains the same. This is because although the superheat is changed, the cooling conditions are not changed, and the heat transfer coefficients in each cooling interval are the same. However, at the same position from the meniscus of the mold, the higher the superheat, the higher the surface temperature of the straightening zone.

The temperature in the core of billet gradually decreases with the continuous casting process under different superheat, as shown in Fig. 6(b). When the distance from the meniscus of the mold is less than 3.59 m, the influence of superheat on continuous casting process is obvious. This is because the cooling intensity at the initial solidification stage cannot act on the core of the billet. When the cooling intensity begins to act on the core, the temperature of the molten steel with higher temperature decreases greatly. When the billet reaches a steady state, the core temperature of the same billet position is higher with the increase of superheat. When the solidification is completed, the distance from the solidification end to the meniscus is 6.21 m, 6.34 m, 6.48 m, 6.62 m, and 6.75 m, respectively when the superheat is 10 °C, 20 °C, 30 °C, 40 °C, and 50 °C, and the length difference is 0.13 m, 0.14 m, 0.14 m, and 0.13 m, respectively. Figure 6(c) shows the change curve of the solid/liquid phase front position during the continuous casting process of the billet at different superheats. With the increase of superheat, at the same position of the billet, the

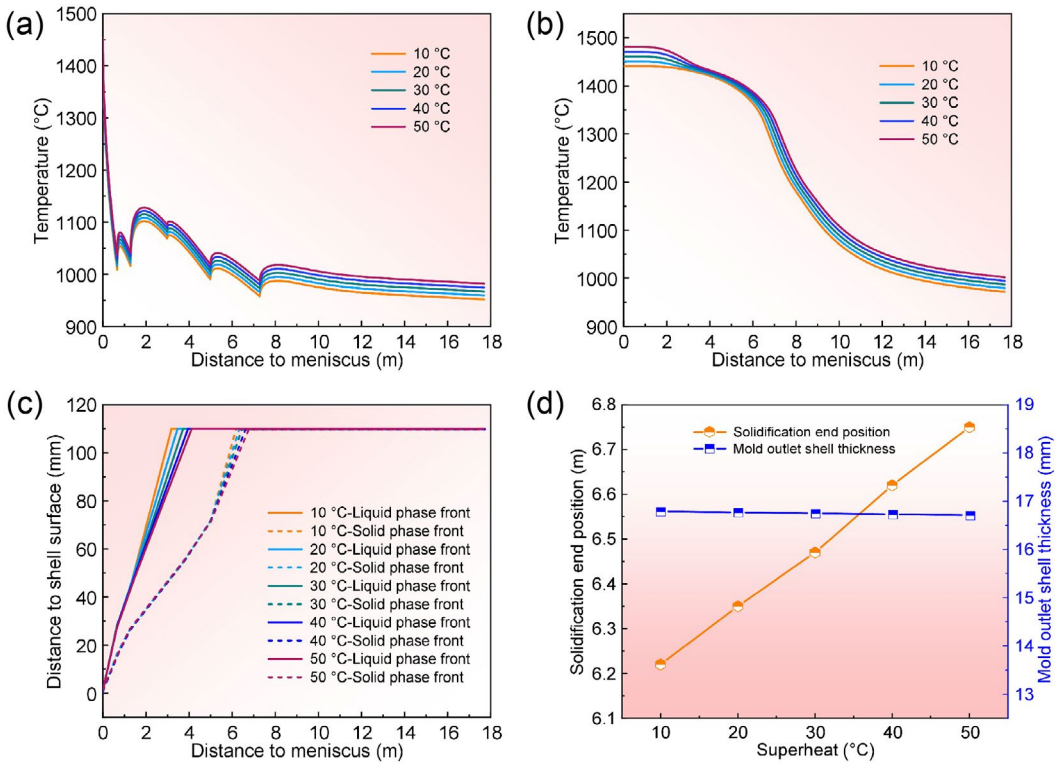

Fig. 6: Effect of superheat on solidification process of continuous casting billet: (a) temperature change of surface center; (b) temperature change of billet core; (c) change of solid phase and liquid phase front position; (d) solidification end position and mold outlet shell thickness under different superheat

solid front and liquid front of the billet are closer to the surface of the billet, and the position where the solid front and liquid front disappear is farther away from the meniscus. The higher the superheat, the higher the pouring temperature, the higher the temperature of the liquid phase when the billet reaches the same position, the longer the mushy zone length, and the thinner the solidified shell thickness, as shown in Fig. 6(d).

In summary, according to the analysis of billet temperature and solidification process, when other conditions remain unchanged, the smaller the superheat, the lower the temperature at steady state, the shorter the liquid cavity length, the thicker the shell, but the influence is small. By comparison, under the above single factor conditions, the influence of casting speed on the temperature field and solidification process of continuous casting billet is significantly higher than that of superheat.

3.3 Coupling effect of multi-factor process parameters

Only analyzing the influence of a single factor on continuous casting billet can not accurately determine the optimal process scheme. Therefore, to account for the interactions among multi-factor process parameters, twenty-five orthogonal experimental schemes were designed, as shown in Table 1.

Before evaluating the results, the key metallurgical criteria in the continuous casting process should be considered in combination with the actual production experience. Firstly, the temperature of the billet entering the straightening zone should be controlled above 900 °C[50]. It is mainly due to the lower temperature and the precipitation of the secondary phase, which increases the plastic deformation resistance of the billet while decreases its ductility the plastic deformation ability. Therefore, in this temperature range, it is necessary to avoid straightening of the billet, otherwise cracks will occur due to stress, comprising the quality of the billet. Secondly, the billet is solidified as completely as possible before straightening to prevent cracks. Additionally, the billet must have a certain shell thickness. This is because when the billet exits the mold and enters the secondary cooling zone, a sufficient shell thickness should be guaranteed to prevent billet bulging and breakout. Furthermore, the molten steel should have a certain fluidity during pouring, therefore, the superheat should not be too low. Finally, the proportion of equiaxed grains in the billet structure should be as high as possible, which is beneficial to the improvement of billet performance and the reduction of solidification defects.

According to the key metallurgical criteria, combined with the results of Table 2 and Figs. 7(a)–(b), Cases 3, 4, 5, 9, 12, 13, 16, 17, and 21 schemes have a temperature of less than 900 °C in the straightening area, that is, the green area in Fig. 7. Among them, lower than 900 °C in the straightening area of the Cases 3, 4, 5, and 9 is mainly because the cooling intensity is too high and the casting speed is relatively low, which leads to the long residence time of the billet in the cooling area, and the cooling effect of the billet in the secondary cooling area is significant, so that the temperature is quickly reduced to below 900 °C before entering the straightening area. However, in Cases 12, 13, 16, 17, and 21, the temperature in the straightening area drops below 900 °C is mainly due to the high specific water flow of the secondary cooling system, which leads to the high surface heat transfer

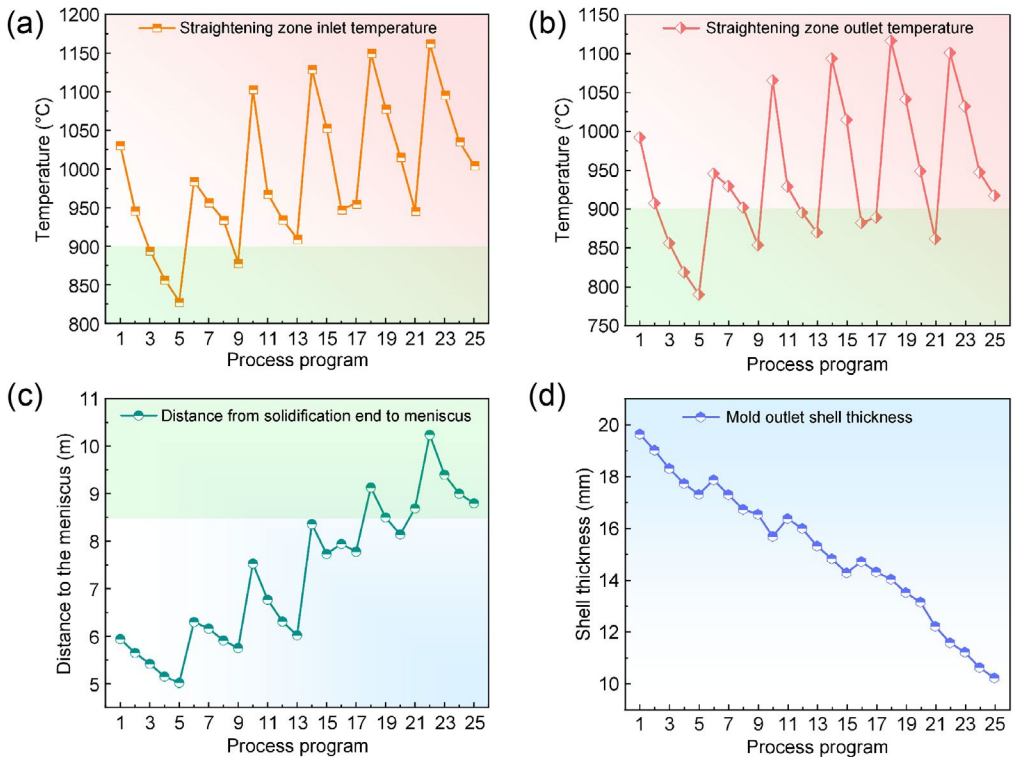

Fig. 7: Influence of multiple process parameters on inlet (a) and outlet (b) temperatures of straightening zone, distance from the solidification end to the meniscus (c), and shell thickness at mold outlet (d)

coefficient of the billet and the greatly enhanced cooling effect. In addition, the lower superheat makes the billet temperature decrease faster. Therefore, no matter the reason, Cases 3, 4, 5, 9, 12, 13, 16, 17, and 21 do not meet the metallurgical criteria for the continuous casting process.

According to Fig. 7(c) and the metallurgical criterion of complete solidification before straightening, the solidification end positions of 25 schemes were analyzed. The distances from the solidification end positions of Cases 18, 19, 22, 23, 24, and 25 schemes to the meniscus are all greater than 8.5 m, which are all in the straightening area. Among them, the schemes of Cases 22, 23, 24, and 25 are mainly because of their high casting speed and insufficient specific water flow. At the same time, the existence of high superheat conditions ultimately leads to the delay of solidification process. The schemes of Cases 18 and 19 have a serious shortage of billet cooling because of the difference between the high casting speed and the low cooling intensity. Thus, Cases 18, 19, 22, 23, 24, and 25 schemes do not conform to the metallurgical criteria.

The thickness of the shell at the outlet of the mold is shown in Fig. 7(d). When the casting speed is fast or the superheat is high, the shell besomes thinner. In order to prevent steel leakage, the casting speed should be slowed down when the superheat increases to ensure the shell thick enough at the outlet of the mold. Based on the previous analysis results, a comprison of Cases 1, 6, and 11 under the same superheat conditions reveals that casting speed has a greater influence on the solidification end position than secondary cooling water. In order to select the best process parameters, considering the solidification end position and the shell thickness, the Cases 10, 14, 15, and 20 with a relatively large distance from the solidification end to the meniscus are continued to be removed. The results of these cases show that the solidification end is closer to the straightening zone, and in the actual production process, a certain margin needs to be set aside for the instability of production. Considering the adverse effects caused by low superheat such as nozzle blockage, mold liquid surface crusting, insufficient melting of mold powder, and inclusion floating, as well as the production efficiency, Cases 7 and 8 are the optimal schemes. The optimal process parameters are a casting speed of 0.9 $m \cdot min^{-1}$, a superheat of 20–30 °C, and a specific water flow of 0.3–0.4 $L \cdot kg^{-1}$.

3.4 Experimental result analysis

Based on the simulation and optimization of multi-process parameters of continuous casting, the experimental verification was carried out in combination with the actual production, the results are shown in Fig. 8. The continuous casting process parameters used in Fig. 8(a) are a casting speed of 0.9 $m \cdot min^{-1}$, a superheat of 30 °C and a specific water flow of 0.2 $L \cdot kg^{-1}$. In Fig. 8(b), the parameters are a casting speed of 0.9 $m \cdot min^{-1}$, a superheat of 20 °C, and a specific water flow of 0.3 $L \cdot kg^{-1}$. After optimization the overall cross-section structure of the continuous casting billet shows a large equiaxed grain zone, and the grain size is reduced.

The columnar-to-equiaxed transition (CET) mechanism of continuous casting billet section mainly lies in the competition of grain nucleation and growth and solute redistribution[51-54]. The growth of columnar crystals depends on the unidirectional heat flow condition, while the formation of equiaxed crystals requires sufficient undercooling and free crystal nucleus. When the temperature gradient at the solidification front

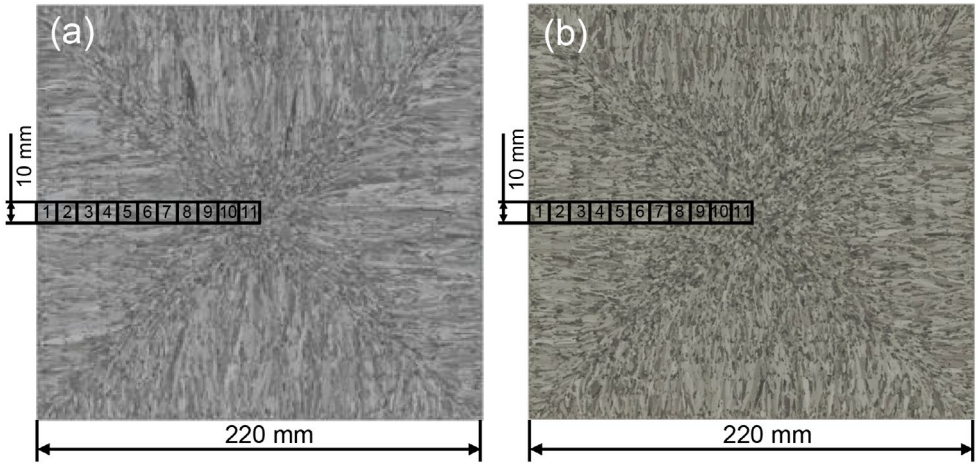

Fig. 8: Billet cross-section structure before (a) and after (b) process parameter optimization, numbers 1–11 in diagram represent sampling position of section structure

decreases to a critical value, equiaxed grains begin to dominate growth[55, 56]. Comparing the process parameters before and after optimization, the superheat is reduced and the secondary cooling specific water flow is increased, that is, the improvement of billet quality is mainly attributed to the synergistic optimization of superheat and secondary cooling specific water flow. The main mechanism is that the increase of specific water flow enhances the supercooling degree and promotes the grain nucleation. At the same time, the decrease of superheat reduces the temperature gradient of the billet section and synergistically promotes the nucleation and growth of equiaxed grains.

Figure 9 shows the cross-section structure of the billet before the optimization of process parameters. It can be seen that there are obvious shrinkage and crack defects in the center of the continuous casting billet. Combined with the previous simulation results, it can be inferred that under the continuous casting process conditions, due to the low secondary cooling water ratio, under the same casting speed conditions, the mushy zone in the solidification process will be longer, resulting in insufficient feeding at the end of solidification, and cracks will be generated under the action of shrinkage stress.

Figure 10 shows the cross-section structure of the billet after the optimization of process parameters. It can be seen that the surface of the billet is fine dendrite, the center is equiaxed crystal, containing residual ferrite, no obvious cracks, the number and size of shrinkage defects are greatly reduced, and the quality of the billet is higher.

Based on the solidification structure of continuous casting billets, the subsequent process in the preparation of seamless tubes was further considered. Figure 11 shows the hot rolled microstructure, as well as the Nb element distribution, before and after the optimization of process parameters. It can be seen that the microstructure recrystallizes to form equiaxed austenite grains during the hot rolling process. However, according to the hot rolling structure before optimization shown in Figs. 11(a–f), it can be clearly observed that a large number of coarse niobium compounds distribute linerly throughout the austenite grains and grain boundaries. These niobium compounds are mainly derived from the precipitation during the solidification process. Due to the extremely low solute equilibrium distribution coefficient of Nb element in austenitic stainless steel, it is easy to segregate and precipitate at the grain boundary during the solidification process, resulting in the formation of coarse niobium compounds[57-59]. Due to the heredity of the structure and the extremely low solid solubility of Nb element, the niobium compounds cannot be dissolved during the high temperature hot rolling process, showing a linear distribution characteristic, which easily cause stress concentration in the subsequent seamless pipe piercing process, resulting in crack initiation. The hot-rolled microstructure after optimization of process parameters shown in Figs. 11(g–i) shows that the distribution of niobium compounds is more uniform and the size is smaller, which can significantly reduce the stress concentration caused by severe plastic deformation in the subsequent hot piercing process. The increase of the secondary cooling water ratio can increase the cooling rate of the solidification process of the continuous casting billet, and inhibit the segregation of the Nb element and the precipitation of the niobium compound to a certain extent. At the same time, the increase of the central equiaxed crystal zone also further makes the distribution of the niobium compound more uniform.

Figure 12 indicates the inner wall morphology and microstructure of the seamless tubes obtained by the same hot rolling and piercing process using the billet before and after the optimization of process parameters. For the hot piercing structure obtained before the optimization, there are long cracks in the inner wall. It can be clearly seen by scanning electron microscopy that there are a large number of large niobium compounds distributed around the cracks. For the billet after the optimization, the quality of the inner wall of the seamless tube obtained by hot rolling and hot piercing process is good, and there are no obvious microcracks in the microstructure. The size of niobium compounds is small and their distribution is more uniform. Therefore, the aggregation distribution of coarse niobium compounds is the direct cause of crack initiation and propagation in the large deformation process of hot piercing of seamless tubes.

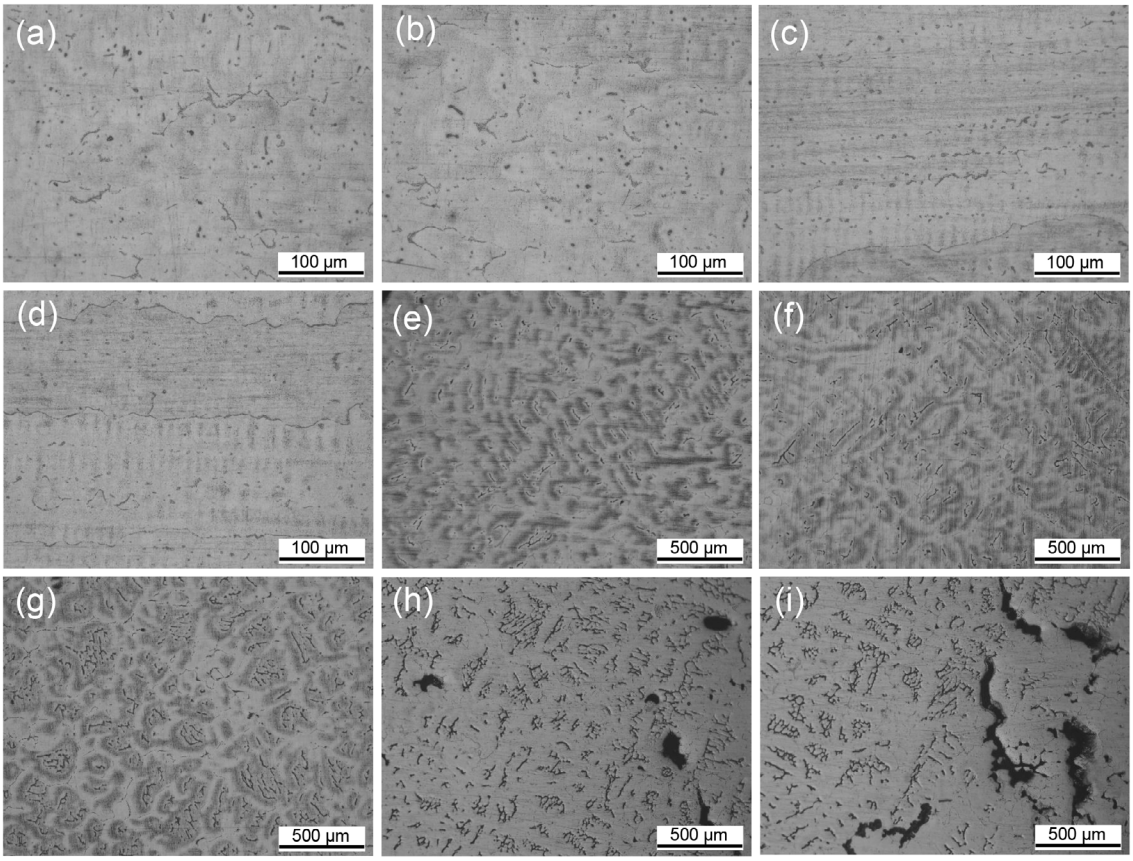

Fig. 9: Cross-section microstructure before optimization of process parameters: (a)–(b) fine grain zone; (c)–(d) columnar crystal zone; (e)–(f) columnar crystal-equiaxed crystal transition zone; (g)–(i) equiaxed crystal zone in center

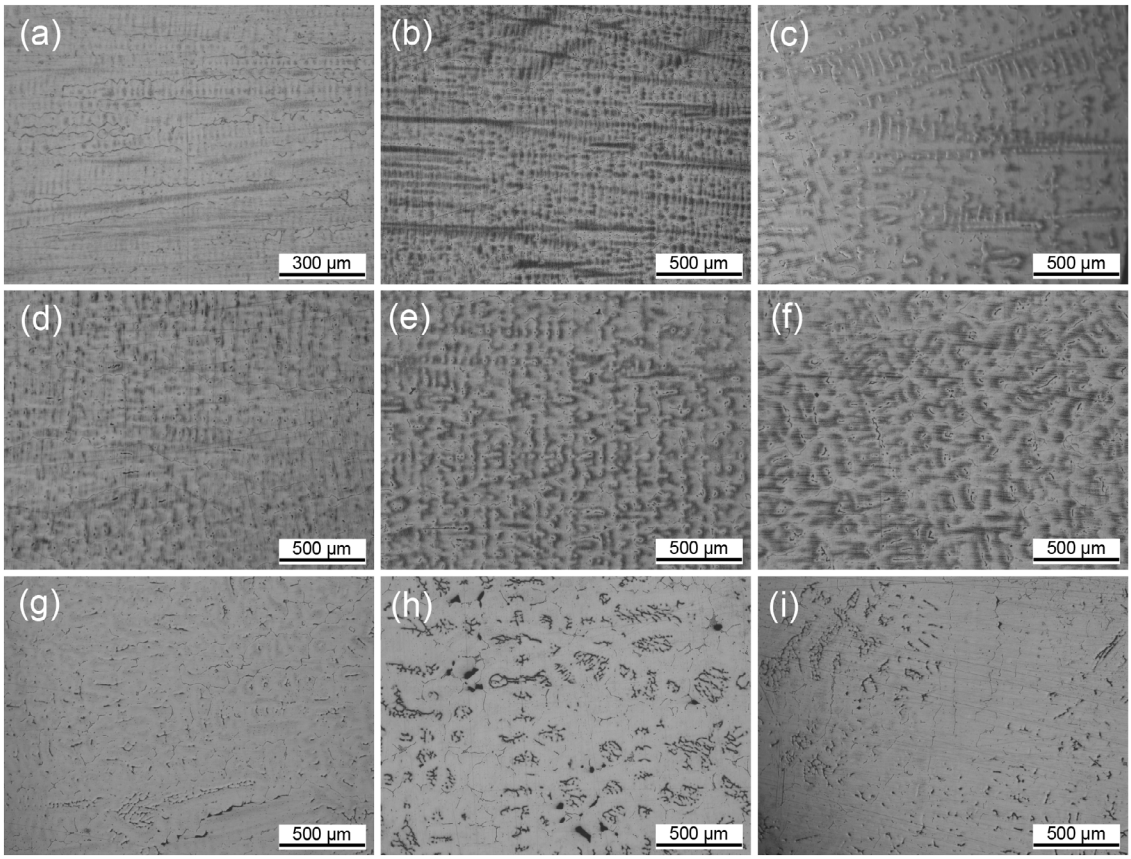

Fig. 10: Cross-section microstructure after optimization of process parameters: (a) near-surface area containing fine grain zone on surface; (b)–(d) columnar crystal zone; (e)–(i) columnar crystal-equiaxed crystal transition zone and central equiaxed crystal zone

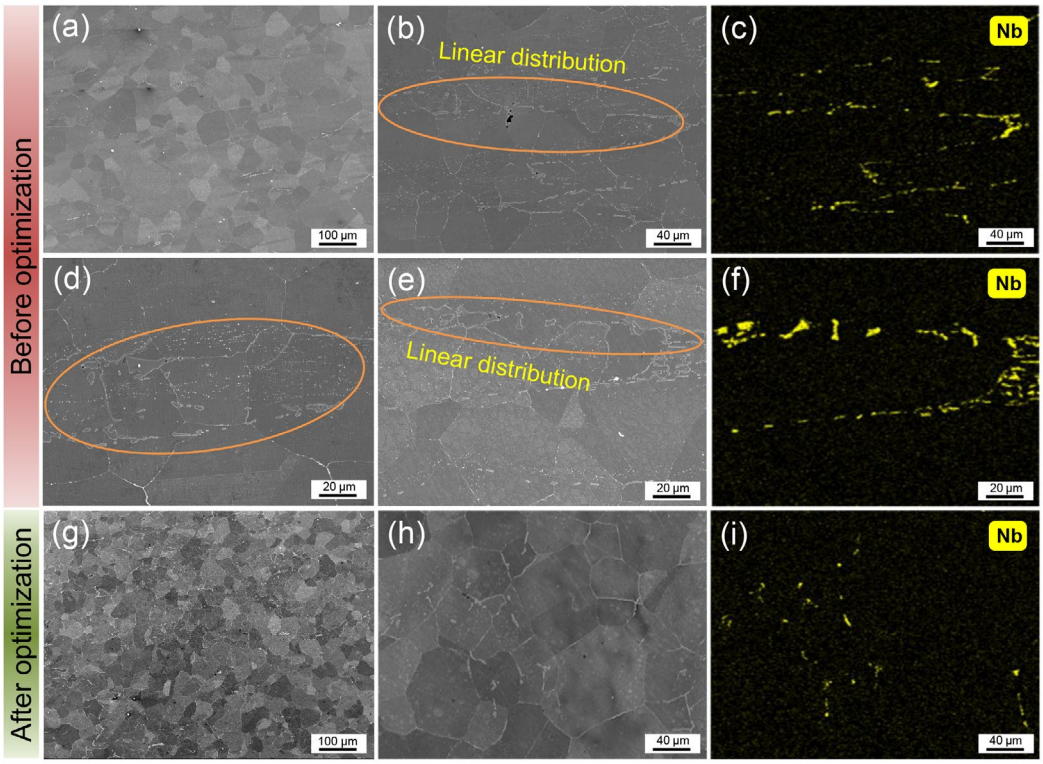

Fig. 11: Hot rolled microstructure before (a)–(f) and after (g)–(i) optimization of continuous casting process parameters

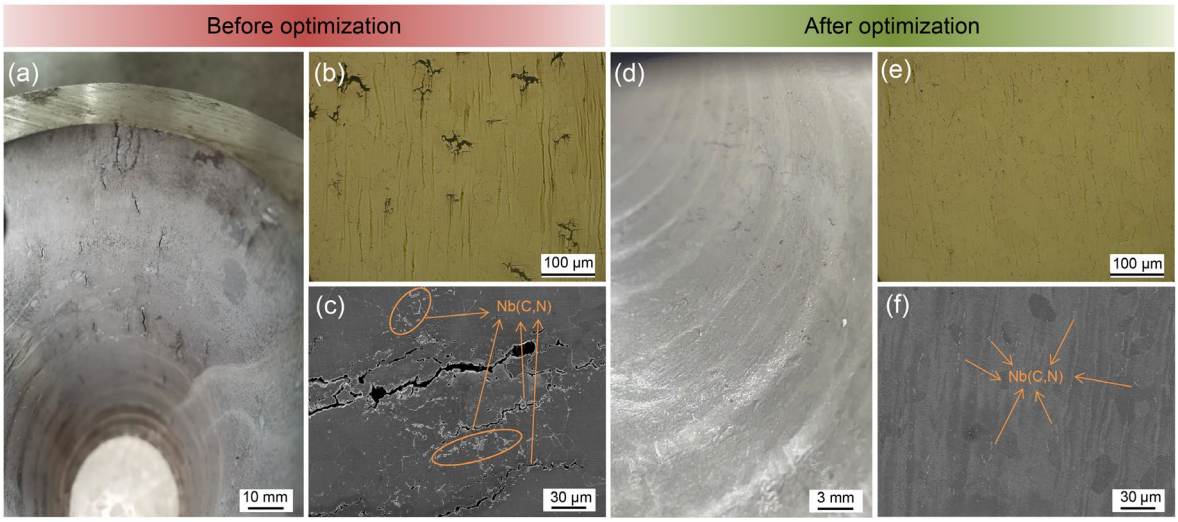

Fig. 12: Morphology and microstructure of inner wall of seamless pipe before (a)–(c) and after (d)–(f) optimization of continuous casting process parameters

In summary, it can be obtained that S30432 Nb-containing steel is easy to form a large number of unevenly distributed and large-sized primary niobium compounds during continuous casting and solidification, which are precipitated between dendrites. After the subsequent hot rolling process, these large primary niobium compounds still exist, and a large number of niobium compounds distributed along the grain boundary are formed after recrystallization. During the process of large plastic deformation of hot piercing, stress concentration is easy to occur around the niobium compounds that are continuously distributed at the recrystallized grain boundary, resulting in crack initiation and propagation. Through the optimization of continuous casting process parameters, the decrease of superheat and increase of secondary cooling specific water flow are beneficial to improve the nucleation density, promote the CET transformation, increase the equiaxed grain zone, and improve the distribution and segregation of Nb element and niobium compound. Finally, continuous casting billets and seamless tubes with few defects or even no defects are obtained.

4 Conclusions

(1) When considering the influence of a single factor, the increase of casting speed or superheat will lead to the increase of mushy zone length. Under simulated conditions,

the influence of casting speed on the solidification process is greater than that of superheat.

(2) The optimal S30432 continuous casting process parameters are a casting speed of 0.9 $m \cdot min^{-1}$, a superheat of 20–30 °C, a specific water flow of 0.3–0.4 $L \cdot kg^{-1}$. The optimized process parameters were used to verify the production experiment, and high-quality continuous casting billets and seamless steel tubes were obtained.

(3) Compared with the microstructure before optimization, the synergistic effect of the lower superheat and higher secondary cooling specific water flow after parameter optimization promotes the grain refinement and expands equiaxed crystal zone in the cross-section of the billet. It also improves the Nb segregation and Nb compounds distribution.

(4) The enrichment of coarse niobium compounds is the direct cause of crack initiation and propagation in the inner wall of S30432 seamless tubes during the deformation process of hot piercing.

Acknowledgments

This research project was supported by the National Natural Science Foundation of China (Nos. U25A20282, U23A20628, 52375394, 52305429) and the Major Project of Science and Technology in Shanxi (Nos. 202501050201012, 202301050201004).

Conflict of interest

Prof. Yu-hong Zhao is an EBM of *CHINA FOUNDRY*. She was not involved in the peer-review or handling of the manuscript. The authors have no other competing interests to disclose.

References

[1] Bhiogade D. Ultra supercritical thermal power plant material advancements: A review. J. Alloys Metall. Syst., 2023, 3: 100024.
[2] Jia J, Li H, Du H, et al. Microstructure and oxidation behavior of C-HRA-5 austenitic heat-resistant steel in air at the temperature range of 650–750 °C. Adv. Eng. Mater., 2024, 26(6): 2301622.
[3] Tikhonova M, Belyakov A, Kaibyshev R. Effect of aging on secondary phases and properties of an S304H austenitic stainless steel. Mater. Sci. Eng. A, 2023, 877: 145187.
[4] Xie A, Chen S, Jiang H, et al. Effects of Nb content and homogenization treatment on the microstructure and mechanical properties of cast austenitic stainless steel. Acta Metall. Sin., 2025, 61(7): 1035–1048.
[5] Liu W, Zhang R, Wu X, et al. Multi-scale simulation of grain evolution during indirect squeeze casting with considering solute suppressed nucleation and externally solidified crystals. J. Mater. Process. Technol., 2025, 342: 118944.
[6] Gao X, Ba W, Wang C, et al. Quantitative influence of solidification path on solute micro-segregation and inclusion precipitation in the solidification process of rail steel. J. Mater. Res. Technol., 2025, 34: 959–971.
[7] Gao X, Ba W, Wang Z, et al. Study of the solute micro-segregation behaviour of bainite rail steel in the continuous casting process. J. Mater. Res. Technol., 2024, 29: 751–763.
[8] Yao C, Wang M, Ni Y, et al. Numerical study on the effect of different spray characteristics of casting nozzles on W-shape solidification and segregation during continuous casting of slabs. Int. J. Heat Mass Transfer., 2024, 218: 124803.
[9] Liu X, Song J W, Wang X, et al. Prediction on the solidification behavior of AA6005 aluminum alloys produced by inclined twin-roll casting: A finite element analysis. J. Mater. Res. Technol., 2024, 29: 2405–2413.
[10] Chen K, Yuan L, Gu Q, et al. Insights into clogging behavior of Al_2O_3-C and ZrO_2-C submerged entry nozzle during continuous casting of ultra-low carbon steel. Corros. Sci., 2025, 246: 112777.
[11] Qiao T, Zhang Y, Cheng G, et al. Failure analysis of nozzle clogging during Super304H stainless steel continuous casting production. Eng. Failure Anal., 2025, 180: 109890.
[12] Cui H, Sun J, Zhang J, et al. Large eddy simulation of novel EMBr effect on flow pattern in thin slab casting mold with multi-port SEN and ultra-high casting speed. J. Manuf. Process., 2025, 133: 448–465.
[13] Zhong H, Guo J, Jiang M, et al. Steel/slag/refractory interfacial reaction and its influence on the cleanliness and control of inclusions in Al-killed steel. Ceram. Int., 2025, 51(24 Part A): 41219–41229.
[14] Liu Q, Wang W, Gao M, et al. Slag rim structure and phase formation mechanism in molds during the continuous casting of high-Mn high-Al steel. Ceram. Int., 2025, 51(5): 5955–5964.
[15] Han Y, Xiao Y, Zhang A Y, et al. Study on influence of lateral liquid feeding into crystallizer on solidification process of copper billets. Int. J. Heat Mass Transfer, 2018, 125: 104–115.
[16] Vakhrushev A, Karimi-Sibaki E, Wu M, et al. Magnetohydrodynamics phenomena in continuous casting process under applied electromagnetic braking (EMBr). Int. J. Thermofluids, 2025, 28: 101315.
[17] Li J, Nian Y, Liu X, et al. Application of electromagnetic metallurgy in continuous casting: A review. Prog. Nat. Sci.: Mater. Int., 2024, 34(1): 1–11.
[18] Zhang Z, Wu M, Zhang H, et al. Modeling of the as-cast structure and macrosegregation in the continuous casting of a steel billet: Effect of M-EMS. J. Mater. Process. Technol., 2022, 301: 117434.
[19] Hu J, Zhang Y, Du S, et al. Electromagnetic DC casting of Zn-Sn alloy: Multiphysics transient coupling simulation and experimental investigation. Mater. Today Commun., 2025, 46: 112485.
[20] Zhong Y, Qiang L, Fang Y, et al. Effect of transverse static magnetic field on microstructure and properties of GCr15 bearing steel in electroslag continuous casting process. Mater. Sci. Eng. A, 2016, 660: 118–126.
[21] Zhang Y, Zhang W, Zeng L, et al. Segregation behavior and precipitated phases of super-austenitic stainless steel influenced by electromagnetic stirring. Mater. Today Commun., 2022, 31: 103675.
[22] Wang E, Zhai Z. Growth and transition of dendrites in steel strands under different electromagnetic stirring methods. J. Cryst. Growth, 2024, 642: 127789.
[23] Shi Z, Zhang Y, Zhang G, et al. Effect of electromagnetic stirring current on the microstructure, mechanical and tribological properties of copper/steel bimetal. Mater. Today Commun., 2025, 47: 113126.
[24] Wang X, Wang Z, Liu Y, et al. A particle swarm approach for optimization of secondary cooling process in slab continuous casting. Int. J. Heat Mass Transfer, 2016, 93: 250–256.

[25] Yu Y, Luo X, Zhang H, et al. Dynamic optimization method of secondary cooling water quantity in continuous casting based on three-dimensional transient nonlinear convective heat transfer equation. Appl. Therm. Eng., 2019, 160: 113988.
[26] Klimeš L, Březina M, Mauder T, et al. Dry cooling as a way toward minimisation of water consumption in the steel industry: A case study for continuous steel casting. J. Clean. Prod., 2020, 275: 123109.
[27] Wang Y, Zhang X, Zhang Y, et al. Effects of cooling channel design and roll-end constraints on the thermal deformation in casting rolls. Int. Commun. Heat Mass Transfer, 2025, 164: 108936.
[28] Zhang J, Chen D, Zhang C, et al. Dynamic spray cooling control model based on the tracking of velocity and superheat for the continuous casting steel. J. Mater. Process. Technol., 2016, 229: 651–658.
[29] Yao C, Wang M, Ni Y, et al. Numerical study on the effect of high efficient cooling nozzles and varying cooling intensity on metallurgical transport behaviors during the slab continuous casting. J. Mater. Res. Technol., 2024, 31: 3812–3824.
[30] Ji C, Di X, Liu X, et al. Multi-field coupling analysis of twin-roll casting process for achieving thin aluminum strip high-speed casting and fabricating laminated metal cladding materials. Case Stud. Therm. Eng., 2025, 72: 106423.
[31] Tian S, Zhao F, and Liu X. Effects of drawing speed on microstructure and properties of Cu-Ni-Si alloy clad AA8030 alloy composites prepared by continuous casting composite technology. Mater. Today Commun., 2024, 40: 109802.
[32] Song X, Lu J, Wang W, et al. Searching the optimal process parameters via heat and mass transfer study of thin slab continuous casting process: A coupled mathematical approach. Therm. Sci. Eng. Prog., 2025, 63: 103757.
[33] Pan D, Zhong H, Guo Q, et al. Research on solidification behavior of a high Mn steel during continuous casting based on solidification characteristic unit analysis. Mater. Lett., 2022, 327: 133028.
[34] Zhong H, Wang R, Han Q, et al. Solidification structure and central segregation of 6Cr13Mo stainless steel under simulated continuous casting conditions. J. Mater. Res. Technol., 2022, 20: 3408–3419.
[35] Li D, Su Z, Marukawa K, et al. Simulation on effect of divergent angle of submerged entry nozzle on flow and temperature fields in round billet mold in electromagnetic swirling continuous casting process. J. Iron. Steel Res. Int., 2014, 21(2): 159–165.
[36] Silva A C E. Using computational thermodynamics to understand the evolution of solidification segregation during steel processing. J. Phase Equilib. Diffus., 2020, 41(4): 522–531.
[37] Zhang Y, Xiao J, Liang J, et al. Effect of rare earth elements on the segregation behavior and microstructure of super austenitic stainless steel. J. Mater. Res. Technol., 2022, 19: 20–29.
[38] Song K, Cao S, Bao Y, et al. Designing hydrogen embrittlement-resistant grain boundary in steel by alloying elements segregation: First-principles calculations. Appl. Surf. Sci., 2024, 656: 159684.
[39] Wang J, Liu Z, Tian H, et al. Inhibition of the second phase precipitation and improvement of intergranular corrosion resistance by boron segregation at the grain boundary of S31254 superaustenitic stainless steel. Corros. Commun., 2024, 15: 1–12.
[40] Ding C D, Jiao Z B, Luan J H, et al. Suppressing hydrogen embrittlement of a CrCoNi medium-entropy alloy by triggering co-segregation of carbon, boron, and Cr. Corros. Sci., 2024, 236: 112232.
[41] Niu M, Chen C, Li W, et al. Atomic-scale understanding of solute interaction effects on grain boundary segregation, precipitation, and fracture of ultrahigh-strength maraging steels. Acta Mater., 2023, 253: 118972.
[42] Gao J, Ma J, Yang S, et al. Grain boundary co-segregation of B and Ce hindering the precipitates of S31254 super austenitic stainless steel. J. Mater. Res. Technol., 2023, 24: 2653–2667.
[43] Ramirez J, Zuñiga F, Samhitha S S, et al. Unraveling the synergistic influence of Nb, V, and Ce on corrosion and high temperature performance of austenitic alloys. J. Mater. Res. Technol., 2025, 36: 6295–6315.
[44] Zhang X, Zhu D, Zhang C, et al. A review of crystal defect-induced element segregation in multi-component alloy steels. Prog. Nat. Sci.: Mater. Int., 2024, 34(5): 840–858.
[45] Wang J, Liu Y, Xi X, et al. Research on the effect of Cu addition on the corrosion resistance of low carbon low alloy steel. J. Mater. Res. Technol.. 2025, 36: 10507–10519.
[46] Shang T, Wang W, Kang J, et al. Precipitation behavior of TiN in solidification of 20CrMnTi under continuous casting conditions. J. Mater. Res. Technol., 2023, 24: 3608–3627.
[47] Gao X, Yang S, and Li J. Effects of micro-alloying elements and continuous casting parameters on reducing segregation in continuously cast slab. Mater. Des., 2016, 110: 284–295.
[48] Wang D, Xie C, Li F, et al. Study on solidification and heat transfer of billet shell in a new-structure high-speed continuous casting mold. J. Mater. Res. Technol., 2024, 33: 3283–3295.
[49] Chen J X. Handbook of continuous cast steel. Beijing: Metallurgical Industry Press, 1991: 191–194. (In Chinese)
[50] Zhai Y, Li Y, Ma B, et al. The optimisation of the secondary cooling water distribution with improved genetic algorithm in continuous casting of steels. Mater. Res. Innovations, 2015, 19: S26–S31.
[51] Hou Y and Cheng G. An investigation of columnar to equiaxed transition and the effect of cooling rate on nucleus density distribution of an industrial Ti and Nb-stabilized ferritic stainless steel. Metall. Mater. Trans. A, 2019, 50(10): 4686–4700.
[52] Yang Y, Shi H, Qu S, et al. Microstructure of nickel-based high-temperature alloys manufactured by directed energy deposition: A review. Int. J. Adv. Manuf. Tech., 2025, 138(7–8): 2781–2817.
[53] Guo D, Hou Z, Peng Z, et al. Quantitative correlation and control strategy for element content fluctuation along casting direction in central area of continuous casting billet. Metals, 2021, 11(3): 452.
[54] Liu P, Wang Z, Xiao Y, et al. Insight into the mechanisms of columnar to equiaxed grain transition during metallic additive manufacturing. Addit. Manuf., 2019, 26: 22–29.
[55] Yu K, Xu L, Zhang Y, et al. Endogenous-exogenous analyses of the solidification structure in 475 mm extra-thick slabs: Columnar-to-equiaxed positioning and effect of strand electromagnetic stirring. Materials, 2025, 18(10): 2179.
[56] Xiong L, Wang C, Wang Z, et al. The interaction between grains during columnar-to-equiaxed transition in laser welding: A phase-field study. Metals, 2020, 10(12): 1647.
[57] Abraham S, Bodnar R, Lonnqvist J, et al. The mechanism for coarse Nb-rich particle formation in steel. Metall. Mater. Trans. A, 2021, 52(9): 3727–3749.
[58] Wang T, Ma J, Dong N, et al. Effect of boron addition on Nb(C, N) refinement and dissolution behavior in Super 304H austenitic heat-resistant steel. J. Mater. Res. Technol., 2025, 36: 1705–1714.
[59] Zhang Y and Zou H. Solidification segregation behavior of Nb-containing 310S steel. J. Iron Steel Res. Int., 2022, 30(1): 82–87.